Enrichment of planetary surfaces by asteroid and comet impacts

Frantseva, Kateryna

DOI:
10.33612/diss.100695383

4. Exogenous delivery of water to Mercury

Kateryna Frantseva, David Nesvorný, Michael Mueller,
Floris F.S. van der Tak, Inge Loes ten Kate
Icarus, under review

Highlights

- The water ice found in Mercury's craters may have been delivered after planet formation.
- Our simulations indicate that impacts of dust particles, asteroids, and comets provide enough water to explain the radar and MESSENGER data.
- Dust is the biggest supplier of water to Mercury, while comets and asteroids contribute at the few % level.
- Endogenic sources of water are possible but not necessary to explain the data.

Abstract

Radar and in-situ observations show the permanently shadowed regions around Mercury's North Pole to contain water ice and complex organic material. One possible source of this material are impacts by interplanetary dust particles (IDPs), asteroids, and comets.

We have performed numerical simulations of the gravitational dynamics of asteroids and comets over the past few Myr, checking for impacts with Mercury. We use the N-body integrator `RMVS/Swifter` *to propagate the Sun and the eight planets from their current positions. Separately, we add comets and asteroids to the simulations as massless test particles, based on their current orbital distributions. Asteroid impactors are assigned a probability of being water-rich (C-class) based on the measured distribution of taxonomic types. For comets, we assume a constant water fraction. For IDPs, we use a dynamical model to compute the dust flux on Mercury. Relative to previous work on asteroid and comet impacts (Moses et al., 1999), we leverage 20 years of progress in minor body surveys.*

Immediate post-impact ejection of impactor material into outer space is taken into account as is the migration efficiency of water across Mercury's surface to the polar cold traps.

We find that asteroids deliver $\sim 1 \times 10^3$ *kg/yr of water to Mercury, comets deliver* $\sim 1 \times 10^3$ *kg/yr and IDPs deliver* $\sim 16 \times 10^3$ *kg/yr within a factor of several. Over a timescale of* ~ 1 *Gyr, this is enough to deliver the minimum amount of water required by the radar and MESSENGER observations.*

While other sources of water on Mercury are not ruled out by our analysis, we show that they are not required to explain the lower limits on the observations currently available.

4.1 INTRODUCTION

The presence of water in the permanently shadowed polar regions of Mercury is well established. Through ground-based observations of Mercury bright radar-reflective regions were detected near the poles of the planet (Slade et al., 1992; Harmon & Slade, 1992; Butler et al., 1993; Harmon et al., 1994) that are consistent with water ice (although sulphur and certain silicates could also explain the radar data). Based on the radar observations, Moses et al. (1999) determined the total mass of the ice to be $4 \times 10^{13} - 8 \times 10^{14}$ kg assuming a layer thickness between 2 m and 20 m.

Observations with the Neutron Spectrometer (NS) aboard the MErcury Surface, Space ENvironment, GEochemistry, and Ranging (MESSENGER) spacecraft (Lawrence et al., 2013) demonstrated that the radar-bright deposits in the North polar region consist of water ice. NS was not sensitive to the South polar region due to the eccentric spacecraft orbit. Specifically, NS observations identified a hydrogen-rich layer associated with water ice of unknown thickness, covered by a less hydrogen-rich layer (less than 25 weight % water-equivalent hydrogen) with a thickness between 0.1 and 0.3 m. Lawrence et al. (2013) adopted an ice layer thickness between 0.5 m and 20 m, where the lower limit follows from the models of surface modification processes (Crider & Killen, 2005) and the upper limit is estimated from models of radar scattering (Butler et al., 1993).

Additional MESSENGER observations using the Mercury Laser Altimeter (MLA) and the Mercury Dual Imaging System (MDIS) allowed both polar regions to be mapped three-dimensionally, and the area of the permanently shadowed regions to be measured: $(1.25 - 1.46) \times 10^{10}$ m^2 around the north pole and $(4.3 \pm 1.4) \times 10^{10}$ m^2 around the south pole (Chabot et al., 2012; Neumann et al., 2013).

Combining these two sets of MESSENGER results, and assuming that radar-reflective regions in Mercury's South polar region are also dominantly water ice with the same layer thickness as in the North, the MESSENGER observations imply a total water mass at Mercury's poles of 2.1×10^{13} to 1.4×10^{15} kg (Lawrence et al., 2013), consistent with the interpretation of ground-based radar observations by Moses et al.. Independently, Eke et al. (2017) derive an upper limit of $\sim 3 \times 10^{15}$ kg from MLA observations of craters.

Different ideas have been presented as to the origin of Mercury's water ice. Endogenous sources such as volcanic activity, crust and mantle outgassing, interaction of surface rocks with solar wind might have played a role in the formation of the bright and dark deposits on the surface of Mercury (Potter, 1995). Nittler et al. (2017) suggest that Mercury's polar

deposits include some fraction of material derived from volatiles outgassed from Mercury's interior, potentially caused by volcanic resurfacing (Wilson & Head, 2008; Head et al., 2009; Prockter et al., 2010; Denevi et al., 2013; Ostrach et al., 2015).

On the other hand, water has been delivered from outside of Mercury. In the current Solar System, plausible impactor populations with meaningful water content would be both macroscopic bodies (asteroids and comets) and microscopic impactors (Interplanetary Dust Particles, IDPs). Frantseva et al. (2018) showed that such impacts may be the source of organic material found on the surface of Mars. Could Mercury's water ice have been deposited in a similar fashion?

Water ice can have accumulated in Mercury's polar cold traps since the end of the Late Heavy Bombardment ~ 3.5 Gyr ago (Moses et al., 1999) or, equivalently for our purposes, the end of the formation of the terrestrial planets according to the accretion tail scenario (Morbidelli et al., 2018). This idea is reinforced by more recent thermal modelling, demonstrating that the permanently shadowed regions are cold enough to keep water ice thermally stable for billions of years (Paige et al., 2013). Water ice deposited on other parts of Mercury's surface is unstable against sublimation; water vapour will diffuse across the surface until it either re-condensates at a polar cold trap or is dissociated by solar ultraviolet radiation and lost to space. Between $\sim 5 - 15\%$ of the water deposited across Mercury's surface will reach the polar cold traps (Butler et al., 1993; Butler, 1997); observational evidence for this diffusion process occurring on the surface of the Moon has recently been presented by Hendrix et al. (2019).

Water delivery by impacts of IDPs, asteroids, and comets has been studied in the past, but questions remain. Moses et al. (1999) estimated the water flux due to impacts of asteroids and comets in the last 3.5 Gyr using a Monte Carlo simulation to generate fictitious comets and asteroids, basing themselves on the populations known at the time and (large) correction factors accounting for observational incompleteness. They find that impacts from Jupiter-family comets can supply $(0.1 - 200) \times 10^{13}$ kg of water to Mercury's polar regions (corresponding to ice deposits $0.05 - 60$ m thick), Halley-type, i.e., long-period comets can supply $(0.2 - 20) \times 10^{13}$ kg of water to the poles ($0.07 - 7$ m of ice), and asteroids can provide $(0.4 - 20) \times 10^{13}$ kg of water to the poles ($0.1 - 8$ m of ice). In order to calculate the IDP ($10 - 500\,\mu$m,) flux on Mercury they extrapolated the current terrestrial influx of IDPs to that at Mercury. The continuous IDP flux on Mercury within the last 3.5 Gyr would deliver $(3 - 60) \times 10^{13}$ kg of water ice to the permanently shaded regions at Mercury's poles (equivalent to

an average ice thickness of $0.8 - 20$ m). More recently, for particles in the size range of $5 - 100\,\mu$m, using a numerical code that takes into account the gravitational interaction with all planets and non-gravitational forces such as the Poynting-Robertson drag and the solar wind drag, Borin et al. (2017) have estimated the total impact flux to be 1.97×10^8 kg/yr, 20 times higher than the estimate by Moses et al. and 5 times larger than the flux on Earth (Love & Brownlee, 1993). Another study of the dust environment around Mercury has been done by Pokorný et al. (2018) for particles in the size range of $10 - 2000\,\mu$m. The total dust flux following from the study is 4.4×10^6 kg/yr, similar to Moses et al. and two orders of magnitude less than Borin et al.. The estimate of Borin et al. appears implausibly high, seeing in particular that the Earth's impact cross-section is $\simeq$7 times larger than that of Mercury (so Earth should receive more IDPs than Mercury, not less).

Given the large discrepancy between the existing estimates, and their large uncertainty due to observational incompleteness, we aim to update the asteroid, comet, and dust impact rates on Mercury based on the most recent catalogues of minor bodies, leveraging the results of nearly 20 years of search programs for asteroids and comets since Moses et al. (1999). First, we study the rates at which comets and asteroids impact Mercury in the current Solar System and we derive the corresponding water delivery rates. We do so using N-body codes modelling the motions of asteroids and comets under the gravitational influence of the Sun and the planets while checking for impacts. These models are described in Section 4.2 together with the derived impact rates. Also, we use the ZoDy model from Nesvorný et al. (2010, 2011a,b) to calculate IDP accretion on Mercury in Section 4.3. In Section 4.4, we calculate the corresponding water delivery rates on Mercury's surface. As discussed above, a fraction of the water will be lost to space immediately after impact, as well as during migration to the poles; this fraction is estimated in Section 4.5. The implications of our findings are discussed in Section 4.6.

4.2 GRAVITATIONAL DYNAMICS OF ASTEROIDS AND COMETS

To study Mercury impact rates in geologically recent times we performed numerical simulations of the gravitational dynamics of the current Solar System. Our model accounts for the gravity of the Sun plus the eight planets Mercury to Neptune. Asteroids and comets are added as different sets of passive test particles, i.e., their gravity is neglected. Non-gravitational

forces are also neglected. We integrate forward in time over Myr timescales. Over these timescales, the current Solar System is close to a steady state, even when accounting for the non-gravitational Yarkovsky effect, so we can assume impact rates to be constant with time (see below for a cross-check on this assumption).

To model the gravitational dynamics, we use the N-body integrator RMVS that corresponds to the RMVS3 version of Swift (Regularized Mixed Variable Symplectic; Levison & Duncan, 1994). The code models the motion of one gravitationally dominant object (Sun) and N massive objects (in our case: $N = 8$) under the influence of their mutual gravity. Test particles move passively under the influence of the combined gravitational potential of the Sun and the planets. The algorithm handles close approaches by performing a time step regularisation by reducing the time step by a factor of 10 at 3.5 $R_{\rm Hill}$ and by another factor of 3 at 1 $R_{\rm Hill}$.

In order to check for impacts during the simulation the RMVS integrator checks if a test particle and planet are having, or will have within the next time step, an encounter such that the separation distance, r, is less than some critical radius, the boundary of the encounter region. If this is true the particle is discarded from the simulation. In order to catch all collisions the time step must be small enough that no particle will cross Mercury's Hill sphere, $R = 0.00148$ AU, during a single time step. We have checked that the fastest test particles in our simulations have Mercury encounter velocities around 150 km/s. It will take more than 20 days even for this fastest test particle to cross Mercury's Hill sphere, i.e., more than 20 time steps. Therefore, we are confident to set up the "baseline" time step in our models to 1 day in order to well resolve the 88-day orbit of Mercury and those of Mercury crossers.

Test particles are removed from the simulation once they collide with a planet or with the Sun. Moreover, test particles are considered ejected from the Solar System and discarded when they exceed a user-provided heliocentric distance. These values are set separately for asteroid and comet simulations (see Subsections 4.2.1 and 4.2.2).

4.2.1 Asteroids

To model asteroid orbits we have used the MPCORB catalogue from February 2017 (epoch K172G). The catalogue contains orbital elements for a total of 730,272 asteroids. We culled inaccurate orbits based on single-epoch data, leaving us with 618,078 asteroids to model. We performed our simulations for 10 Myr forward in time in order to get a sufficient number of impactors while avoiding depletion of the impactor orbits. After

reaching a heliocentric distance of 1,000 AU, asteroids were considered ejected from the Solar System and discarded.

At the end of the simulation 12,480 asteroids were discarded from the system. 6,719 asteroids collided with the Sun, 4,609 asteroids were ejected and 1,152 asteroids collided with the planets. Among the latter, 37 asteroids collided with Mercury, corresponding to an average Mercury impact rate of 3.7 impacts per Myr. In Figure 4.1, in blue (Simulation 1/K172G) we show the semi-major axes of all 37 impacting asteroids at the start of the simulations. They are distributed between 0.5 AU and 3.5 AU (Mercury's semi-major axis is 0.387 AU) with a peak near 0.7 AU.

As a crosscheck, we have performed two more asteroid simulations using different initial conditions. For the first crosscheck simulation we have used asteroid orbital elements from MPCORB as of July 2016 (epoch K167V) together with planetary positions for the same date, while for the second crosscheck simulation we have used MPCORB as of March 2018 (epoch K183N) for the asteroid orbital elements together with the corresponding planetary positions. 43 and 37 asteroids impacted Mercury during the first and second crosscheck simulation, respectively, consistent with our primary result of 37 impactors within the Poisson noise. The individual asteroids that impact in the first simulation do not impact in the crosscheck simulations and vice versa, which means that our results are valid in a statistical sense, only. We do not identify individual impacts, but we do characterise the population of Mercury impactors.

From here on we will refer to the primary simulation as Simulation 1, to the first crosscheck simulation as Simulation 2 and to the second crosscheck simulation as Simulation 3.

We analysed the number of asteroids impacting Mercury after each Myr of the simulation as shown in Fig. 4.2. In this way we studied the time evolution of the Mercury impactors. We expect the number of impactors to be proportional to time. Any significant violation of our assumptions (e.g., depletion of asteroids on impactor orbits or Yarkovsky drift) would result in a deviation from this. We did find the total number of impactors to increase steadily, within the $\sqrt{N}$ Poisson noise, justifying our assumptions.

4.2.2 Comets

In order to model cometary orbits we have used the MPCORB catalogue from November 2016 which contains 893 comets. Of these, we have used 879 comets whose orbits are calculated for the current epoch. As described in Frantseva et al. (2018), the initial cometary set is too small to draw statistically valid conclusions, therefore we have replaced each

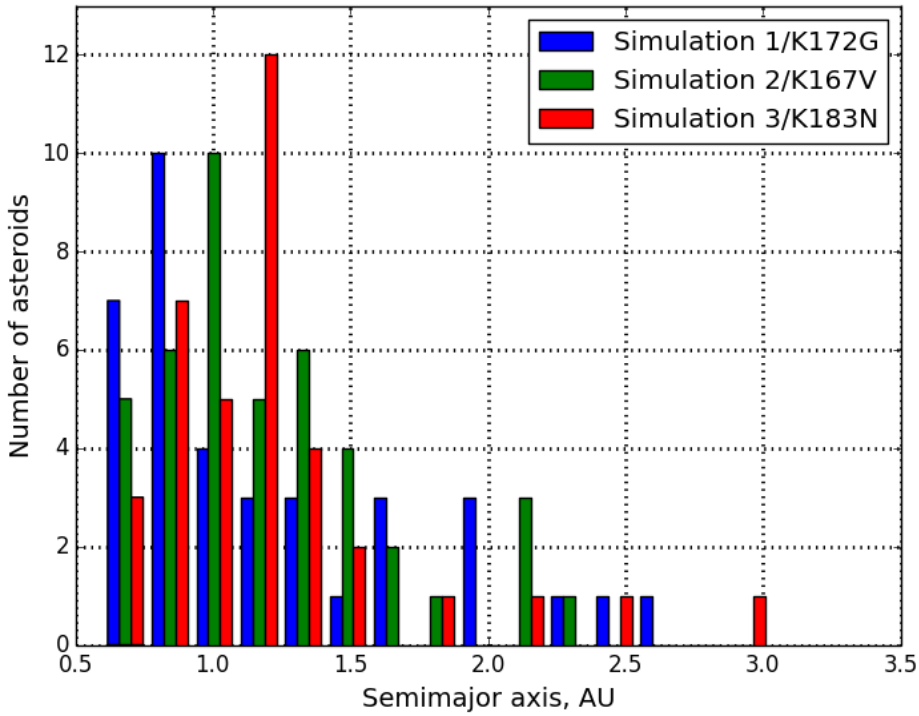

Figure 4.1: Orbital distribution of the Mercury impacting asteroids. Blue bins correspond to the primary simulation, green bins to the first crosscheck simulation and red bins to the second crosscheck simulation. K172G, K167V and K183N stand for February 2017, July 2016, March 2018, which are the corresponding epochs for each simulation .

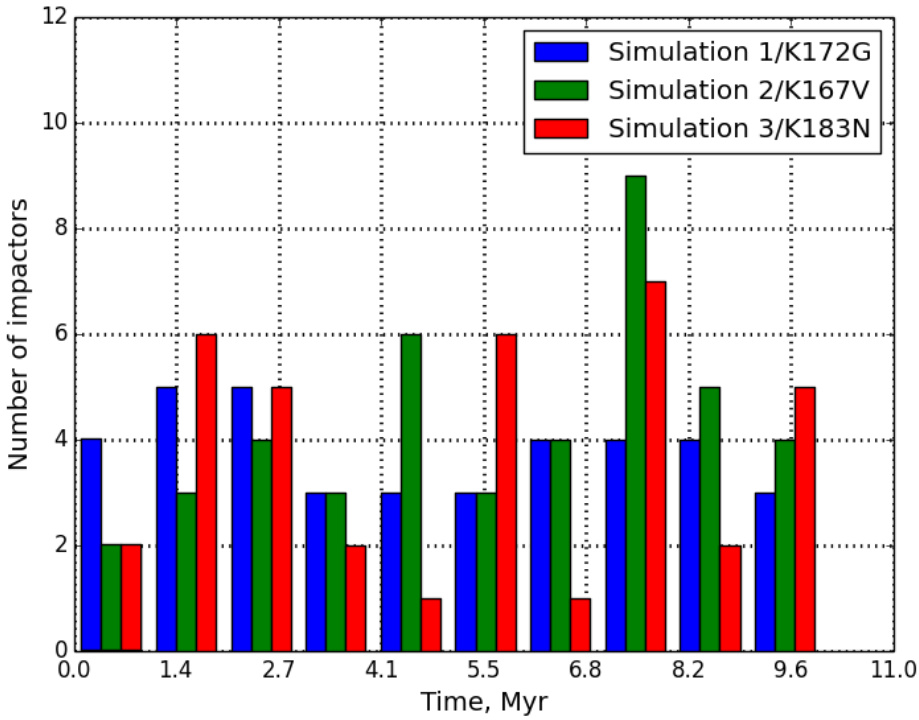

Figure 4.2: Number of asteroids impacting Mercury per 1 Myr. Blue, green and red colours correspond to the primary and the two crosscheck simulations, respectively.

comet with 5000 synthetic "clone" comets with randomised angular orbital elements (the semi-major axis a, eccentricity e, and inclination i values were kept as of the actual comets). Moreover, Mercury's radius was inflated by a factor of 50. The simulation was performed for 0.1 Myr forward in time; this simulation length was chosen to not significantly deplete the comet population over the course of our simulations. A comet was considered discarded from the simulation if it had collided with a planet, with the Sun, or when it reached a heliocentric distance of 125,000 AU. This large threshold value of the heliocentric distance is required by the high eccentricity of some comets.

At the end of the simulation, 76,261 synthetic comets were discarded from the simulation including 3,651 objects that had impacted Mercury. Accounting for cloning of the comets, the inflation of Mercury's radius and the duration of our simulation, this corresponds to $3,651/5,000/2,500/0.1 = 0.0029$ impacts per Myr.

Like in the case of asteroids, we estimated the uncertainty in our comet result through a crosscheck simulation for a different epoch, November 2017. During the crosscheck simulation 3,684 comets impacted Mercury, consistent with our primary result of 3,651 impactors within the $\sqrt{N}$ Poisson noise.

4.3 INTERPLANETARY DUST PARTICLES

We use the ZoDy model (Nesvorný et al., 2010, 2011a) to compute the accretion of IDPs on Mercury. In the ZoDy model, IDPs of different sizes are released from asteroids and comets. Their orbital evolution is followed by an efficient N-body integrator (*Swift*, Levison & Duncan, 1994) until they are ejected from the Solar System, or impact on the Sun or planets. The N-body integrations include the gravitational effects of the Sun and the planets. Due to the small sizes of the dust particles, non-gravitational forces such as radiation pressure, Poynting-Robertson and solar wind drag are also accounted for. The orbit of each particle is saved at 1,000 yr time intervals, thus allowing us to construct a steady state distribution of orbits for individual sizes. For example, for particles from Jupiter-family comets (JFCs), which probably are the most important source of IDPs in the inner Solar System (see below), we follow the orbital evolution of particles with 28 different sizes from 1 μm to 10 mm. Each set of integrations included 10,000 particles of the same size.

In the absence of mutual collisions between particles, the size distribution of particles in space would be defined by their *initial* size

distribution in the source and by their dynamical lifetimes. In the current ZoDy model, the initial size distribution is parameterised by a broken power law with a break at diameter d^*, and differential power indices $\gamma_{\rm S}$ for small particles and $\gamma_{\rm L}$ for large particles. Motivated by the comparison of the ZoDy model with the Long Duration Exposure Facility (LDEF) satellite measurements (Love & Brownlee, 1993; Nesvorný et al., 2011a), we use $d^* \simeq 200$ μm, $\gamma_{\rm S} \simeq -2$ and $\gamma_{\rm L} \simeq -5$. In this case, both the mass and emission cross-section of IDPs are dominated by $d \simeq 200$ μm particles, implying that the mass in micrometeoroids accreted by planets is also dominated by $d \simeq 200$ μm particles.

Once the initial size of the particles is fixed, the orbital integrations are used to compute the size distribution of particles at any location in the Solar System. To do this properly, we account for disruptive collisions between particles, which act to destroy parent particles and generate fragments. It is difficult to fully account for the collisional cascade in an N-body integrator because N can increase enormously when new particles are added. We therefore adopt a standard approach to this problem (e.g., Grun et al., 1985), where the collisional lifetime, $\tau_{\rm c}$, is defined as a function of size and orbit, and used to decide whether a particle is removed. This approach ignores fragments generated by disruptive collisions. A Poisson random number generator is used to determine whether a particle is disrupted (depending on its size and orbital history).

The orbital dependence of $\tau_{\rm c}$ can be determined from first principles (see Nesvorný et al., 2011b, for a discussion). The size dependence, however, is *a priori* unknown and must be treated as a free parameter (or a set of free parameters). In our past work, we used different prescriptions for $\tau_{\rm c}(d)$, including cases from Grün et al. (1985), $\tau_{\rm c}(d) = constant$, and other dependencies where $\tau_{\rm c}$ increases with d. To fit the meteor data on Earth, for example, we found that $\tau_{\rm c} \gtrsim 10^5$ yr for $d > 100$ μm (for a reference orbit with $a = 1$ au and $e = i = 0$).

Nesvorný et al. (2010) used the ZoDy model to determine the relative contribution of asteroid and cometary material to the Zodiacal cloud and the mass in IDPs accreted by the Earth. They found that the mid-infrared (MIR) emission from particles produced in the asteroid belt is mostly confined to within latitudes $b \lesssim 30^\circ$ of the ecliptic. Conversely, the Zodiacal cloud has a broad latitudinal distribution such that strong thermal emission is observed even in the direction of the ecliptic poles. This shows that asteroidal particles can represent only a small fraction (under 10%, e.g., Carrillo-Sánchez et al., 2016) of the Zodiacal cloud emission. Their contribution to the mass accreted by planets can be larger than that 10%, because asteroid IDPs move on low eccentricity and low inclination

orbits, their velocities with respect to planets are lower, and their impact cross-section is therefore strongly enhanced by gravitational focusing.

Based on a detailed comparison of the dynamical model with MIR observations by the Infrared Astronomical Satellite (IRAS) and the Cosmic Background Explorer (COBE), Nesvorný et al. found that $\gtrsim$90% of the zodiacal emission at MIR wavelengths comes from dust grains released by JFCs, and only $\lesssim$10% comes from the long periodic comets. The total mass accreted by the Earth in JFC particles between diameters $D = 5$ μm and 1 cm was found to be $\sim 15 \times 10^6$ kg yr^{-1} (Nesvorný et al. 2011a; factor of 2 uncertainty), which is a large share of the accretion flux measured by LDEF (Love & Brownlee, 1993). Based on these results we consider only IDPs from asteroids and JFCs for our calculations. All other populations, such as long period comets and Kuiper belt, are ignored because previously it has been demonstrated that these dust populations do not contribute much to the accretion on terrestrial planets. In Section 4.4.3, we use the ZoDy model for asteroid and JFC particles to determine the impact flux of IDPs on Mercury (also see Pokorný et al., 2017).

4.4 WATER DELIVERY RATES

In Sections 4.2.1 and 4.2.2, we estimated that Mercury suffers 0.0029 comet impacts per Myr and 3.7 asteroid impacts per Myr. In this section we will convert the impact rates into water delivery rates. Based on the described methods for the IDP flux we will estimate the corresponding water flux on Mercury.

4.4.1 Asteroids

Asteroids are known to be parent bodies of meteorites. We here focus on the carbonaceous chondrite meteorites, which are known to be water and organic rich. Their water content is $\sim 10\%$ by mass, their carbon content is $\sim 2\%$ by mass and their parent bodies are the C type asteroids (National Research Council, 2007; Sephton et al., 2002; Sephton, 2014). By comparison, other taxonomic types contain negligible amounts of water; they are neglected.

To calculate the water delivery rate of the asteroid impacts we use the statistical approach discussed in Frantseva et al. (2018), where each impactor is assigned a probability p_{C} of belonging to the C type depending on its semi-major axis at the start of the simulations. The amount of water

delivered by an asteroid depends on p_{C}, the asteroid mass m_{Asteroid} and f_{Water}, the water content of carbonaceous chondrite meteorites:

$$M_{\mathrm{Water}} = p_{\mathrm{C}} m_{\mathrm{Asteroid}} f_{\mathrm{Water}}. \tag{4.1}$$

The water delivery rate equals the sum over all impactors, divided by the duration of our simulation.

The diameter D of an asteroid is based on the H magnitude (Bowell et al., 1989) and geometric albedo p_V (Pravec & Harris, 2007):

$$D = \frac{1329\mathrm{km}}{\sqrt{p_V}} 10^{-H/5} \tag{4.2}$$

where $p_V = 0.06 \pm 0.01$ (a representative value for C type asteroids, see DeMeo & Carry, 2013, Table 1). Mass follows from diameter adopting an average C type mass density ρ of 1.33 ± 0.58 g/cm^3 (Table 3; Carry, 2012):

$$M = \frac{\pi}{6} D^3 \rho. \tag{4.3}$$

The probability of an asteroid being part of the C type, p_{C}, is estimated based on the initial semi-major axis a of an asteroid at the start of the simulation. For impactors with $a < 2$ AU, we identify p_{C} with the "dark fraction" in the albedo distribution of NEOs as measured by WISE (Wright et al., 2016, dark NEOs are predominantly asteroids of the C class). For the remaining impactors, we use the measured fraction of C types relative to all asteroids derived by DeMeo & Carry (2013), based on NIR spectroscopic surveys. DeMeo & Carry provide two sets of results, before and after debiasing against albedo-dependent survey efficiency, we use the latter. WISE is not subject to such a bias, therefore the C-type fraction for $a < 2$ AU need not be debiased. We adopt p_{C} values of 0.253 for $a < 2$ AU (Wright et al., 2016); 0.0612 for 2 AU $< a <$ 2.18 AU, the DeMeo & Carry value for $a = 2.18$ AU. For $a > 2.18$ AU, we use C-type fractions specified for each 0.02 AU bin in Figure 9 in DeMeo & Carry (2013) (see also Fig. 2 in Frantseva et al., 2018). In practice, the majority of Mercury impactors has $a < 2$ AU, see Fig. 4.1.

Using Equation 4.1, we estimate a rate of water delivery to Mercury due to asteroid impacts of $0.021 \pm 0.009 \times 10^6$ kg/yr, averaged over 10 Myr. The uncertainty is calculated combining the known uncertainties of H magnitude, albedo, and mass density (the uncertainty in p_{C} and water content are neglected).

Simulation	Epoch	Number of impactors	Water flux, 10^6 kg/yr
1	K172G, February 2017	37	0.021 ± 0.009
2	K167V, July 2016	43	0.023 ± 0.009
3	K183N, March 2018	37	0.430 ± 0.190

Table 4.1: For each of our three asteroid simulations we report the epochs at which they were initialised, the resulting numbers of Mercury impacting asteroids, and the corresponding water fluxes.

Using the same method, we also analysed the results of the two crosscheck simulations, Simulations 2 and 3, resulting in a mean value for the water delivery rate of $0.023 \pm 0.009 \times 10^6$ kg/yr and $0.430 \pm 0.190 \times 10^6$ kg/yr, respectively. While Simulation 2 is in good agreement with Simulation 1, Simulation 3 differs by a factor of nearly 20. We attribute this discrepancy to the different size-distribution of the Mercury impactors: the third simulation contained several relatively big impactors of 2-5 km in diameter, while impactors in the primary and first crosscheck simulation were smaller. The largest few impactors dominate the mass budget, leading to large Poisson noise. Moses et al. (1999) report similar mass-flux differences between simulations due to the mass flux being dominated by the largest few impactors. The results of the three asteroid simulations are listed in Table 4.1. We adopt the harmonic mean of the three runs, 0.032×10^6 kg/yr within a factor of four to five, as our final asteroid delivery rate.

Our calculations are based on the present-day catalogues of asteroids and comets, which are known to be incomplete. They are missing the smallest objects that are too faint to be detected. Nevertheless, the largest asteroids will dominate the total flux while the contribution of the undiscovered asteroids is only $\sim$4% as described in Frantseva et al. (2018). Observational incompleteness of asteroid catalogues is therefore uncritical for our purposes.

4.4.2 Comets

The two simulations in Section 4.2.2 agree on the cometary impactor flux on Mercury is ≈ 0.0029 comets per Myr. In order to calculate a water delivery rate to Mercury we need to know the typical comet mass and water content. We assume the typical comet mass to be 3×10^{13} kg following Swamy (2010). Various comet observations suggests the water content to lay in a range of 3% and 90% (Gicquel et al., 2012; Huebner, 2002; Jewitt, 2004; Taylor et al., 2017) and 50% from the comet nucleus modelling (Prialnik, 2002). For our calculations we adopted an average value of 50% due to the diversity of the observed and modelled cometary water content. We estimate the water delivery rate to Mercury to be 0.044×10^6 kg/yr.

As in the case of asteroids, our comet catalogue is observationally incomplete, with a bias against small, faint objects. We neglect that bias for the same reason as for asteroids. Additionally, we are strongly biased against discovering comets with large orbital periods (due to the finite temporal baseline available). Systematic surveys (aimed at discovering potentially hazardous asteroids, but discovering comets as bycatch) started

in the 1990s, so for orbital periods up to 20+ years, our catalogues should be reasonably complete. Those provide the bulk of the water retained on Mercury; longer-period comets hit at very large relative velocity, causing most water to be lost to space (see discussion below). Therefore, observational incompleteness is as uncritical for comets as it is for asteroids.

4.4.3 Interplanetary Dust Particles

Using the methods described in Section 4.3, we determine the ratio of IDP impact fluxes between the Earth (here used as a calibration point) and Mercury. For JFC particles, we find that the IDP flux on Earth should be $\sim$4 times larger than on Mercury, mainly owing to its larger impact cross-section (the Earth's cross-section is $\simeq$7 times larger than that of Mercury). For asteroid particles, the Earth should receive $\sim$15 times the IDP accretion of Mercury, a significantly higher ratio than the one obtained for JFC particles. This difference is probably related to stronger gravitational focusing of asteroid IDPs by the Earth (asteroid IDPs have lower inclinations and lower eccentricities, thus lower impact velocities).

We now need to convert these ratios to absolute impact fluxes. For that we use a calibration from Nesvorný et al. (2011a), who found that Earth accretes $\sim 2 \times 10^7$ kg/yr in JFC IDPs, which is about half of the total input measured by LDEF. If so, Mercury should receive 5×10^6 kg/yr of JFC IDPs.

The computation of asteroid IDP flux on Mercury is more uncertain, because we do not have a reliable calibration of asteroid IDP flux on Earth. For example, if we assume that the asteroid IDPs are responsible for roughly half of the IDP flux measured flux by LDEF, then we can estimate that Mercury should receive only $\sim 10^6$ kg/yr in asteroid IDPs (or $\sim 2 \times 10^6$ kg/yr if asteroid IDPs are responsible for the full flux measured by LDEF). We will adopt $\sim 10^6$ kg/yr as the asteroid IDP flux to Mercury.

We estimate the joint asteroid and comet IDP flux on Mercury to be 6×10^6 kg/yr. Given the uncertainties, our estimate is in good agreement with 4.4×10^6 kg/yr by Pokorný et al. (2018), who used a similar model.

Some fraction of IDPs are anhydrous and some are hydrous. The values of these fractions have been studied in the past. It has been estimated that the hydrous IDPs can be from 1% and up to 75% of the total IDPs (Engrand et al., 1999; Noguchi et al., 2002; Dobrica et al., 2010; Zolensky & Lindstrom, 1992). Here we will use $\sim$ 40% as a conservative proportion of dust particles initially containing water. The water content of the hydrous dust particles was found to be from 1wt% and up to 40wt% (Engrand et al., 1996). We will use 20% water content of the hydrous dust particles.

All told, we estimate that dust particles deliver $\sim 0.5 \times 10^6$ kg/yr within a factor of ~ 2 of water to Mercury.

4.5 WATER SURVIVABILITY

In the previous section we converted impact fluxes of asteroids, comets, and IDPs to the corresponding water fluxes. We have shown that Mercury will receive 0.032×10^6 kg/yr of water from asteroids, 0.044×10^6 kg/yr of water from comets, and 0.500×10^6 kg/yr of water from IDPs.

However, only a fraction of this water will be deposited at the poles. A (possibly large) fraction is lost immediately after impact, as impactor material evaporates, forming a supersonic plume, with some of its water content accelerated beyond escape velocity. The water that is retained by Mercury's gravity will migrate across the surface until it is caught at the poles; in the mean-time, some fraction of it is lost to dissociation.

4.5.1 Water loss at impact

Asteroids and comets just like dust particles hit the surface of Mercury at high relative velocity. All impactors including dust particles reach the surface essentially undecelerated by Mercury's tenuous exosphere, not even small dust grains feel Mercury's exosphere appreciably (Ceplecha et al., 1998; Ceplecha & Revelle, 2005). Impacts on planetary surfaces are a topic of extensive research (see, e.g., Jutzi et al., 2015, for an overview). Impacts cause a (potentially large) fraction of the asteroid, comet and dust material to reach velocities beyond escape velocity immediately after impact, so that material is lost. The fraction of retained impactor material is governed by the relative velocity between impactor and Mercury at the time of impact, the impact speed. Fast impactors will lose most material to space, while material from slower impacts is retained more efficiently. Impact velocity, in turn, depends chiefly on orbital parameters: high e and high i favour high impact velocity.

For asteroids and comets we estimate the relative velocity between impactor and Mercury from the RMVS output just before a test particle (asteroid or comet) is discarded, at the time step where the integrator recognises that the test particle will impact. That time step is much less than one day before the time of impact, the relative velocity obtained from it should be a good approximation for the actual impact velocity. See Fig. 4.3 for a histogram of impact velocities of comets, Fig. 4.4 for asteroids. Most of the particles are seen to impact at velocities of 20-40 km/s.

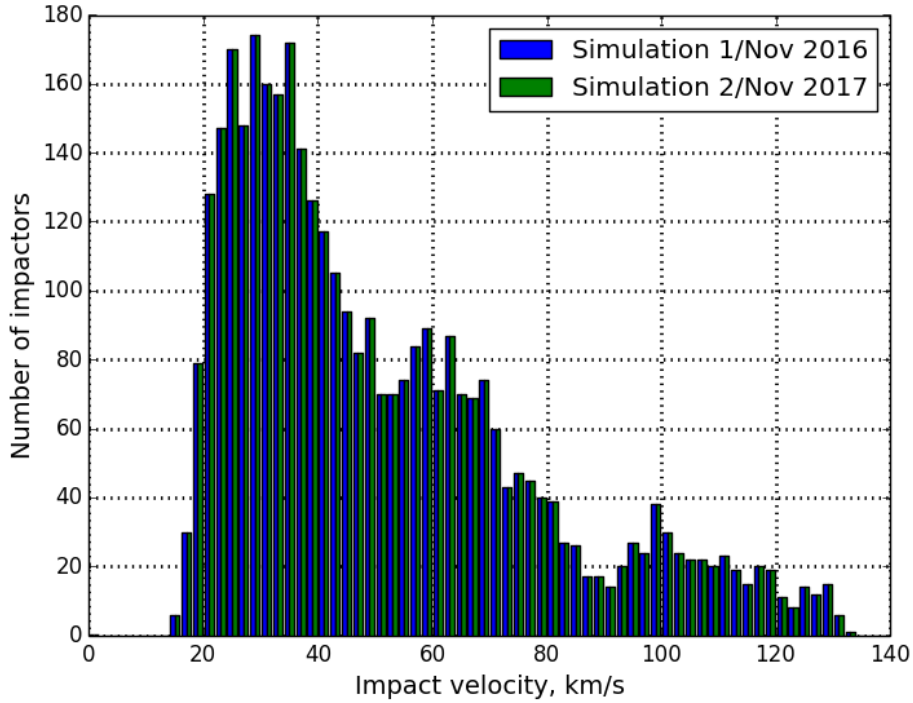

Figure 4.3: Velocities at which comets impact Mercury. Blue bins correspond to the simulation performed using data from MPCORB as of November 2016 and green bins correspond to the simulation performed using data from MPCORB as of November 2017; the distribution in impact velocity is indistinguishable.

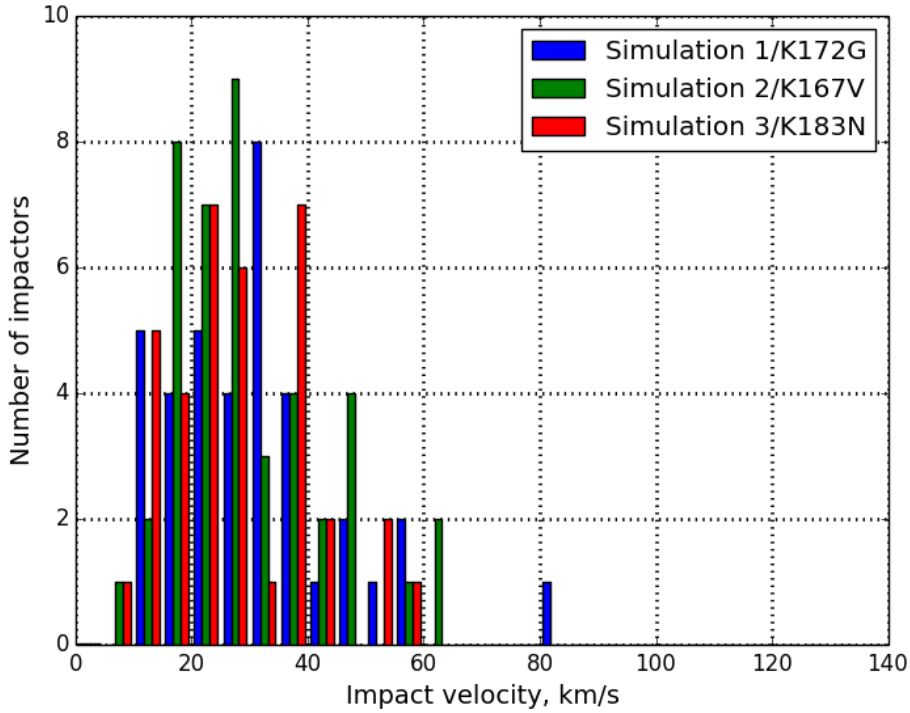

Figure 4.4: Velocities at which asteroids impact Mercury. Blue bins correspond to the primary simulation, green bins correspond to the first crosscheck simulation and red bins correspond to the second crosscheck simulation.

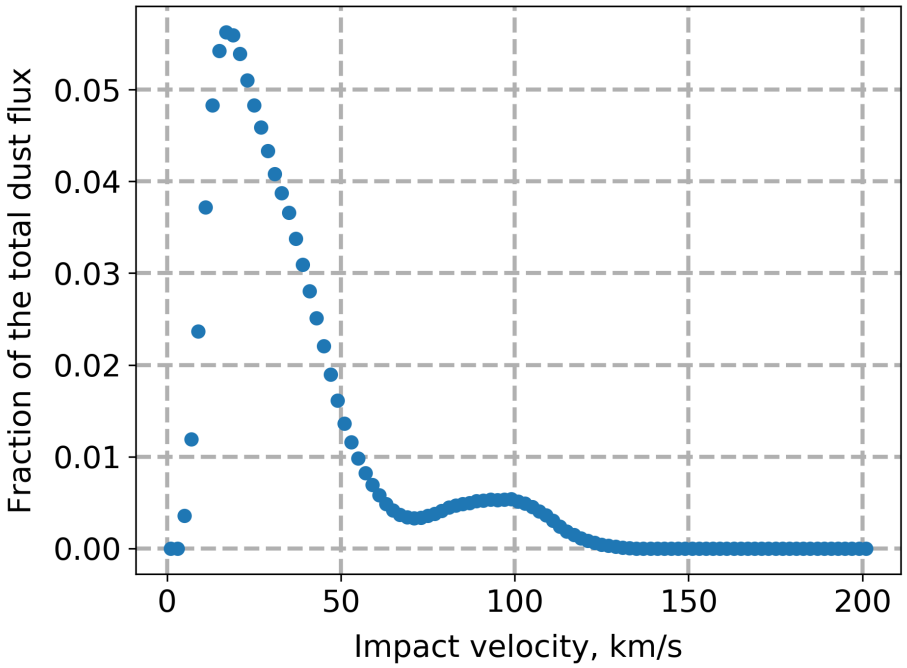

Figure 4.5: Impact velocity distribution of the total dust flux on Mercury (derived from Pokorný et al., 2018, Figure 22).

For the interplanetary dust particles we use a distribution of dust mass flux as function of impact velocity from Pokorný et al. (2018, their Figure 22). In particular, we take their mass influx distribution as a function of Mercury's true anomaly and the impact velocity. We averaged the distribution over Mercury's orbital period as function of impact velocity and normalise it by the total daily dust flux. Fig. 4.5 shows the resulting distribution of the total dust flux on Mercury as function of impact velocity.

To estimate the retained mass fraction of asteroids, comets and dust particles upon impact, scaling laws have been established based on comparison between high-speed impact experiments and numerical simulations. We base our analysis on the formalism developed by Svetsov (2011), which is accurate enough for our purposes. To estimate the fraction of the escaped projectile mass, $\frac{m_p}{m}$, for the impactors with low impact velocities $V \leqslant 15$ km/s, we use their Equation 8:

$$\frac{m_p}{m} = 1 - (0.14 + 0.003V) \ln v_{\text{esc}} - 0.9V^{-0.24}, \tag{4.4}$$

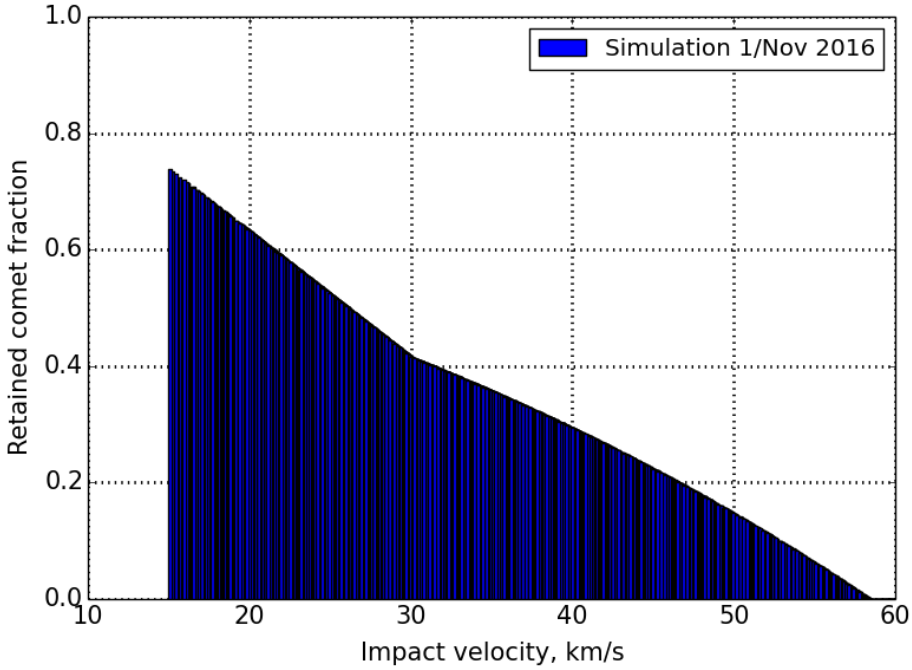

Figure 4.6: Retained mass fraction of each comet impacting Mercury in the first comet simulation. For impact velocities larger than 60 km/s, all impactor material (and hence all water) is lost to space. The retained mass fraction of the impacting comets in the second simulation is indistinguishable from the first simulation and is not plotted here.

while for high impact velocities $V \geqslant 30$ km/s we use their Equation 9:

$$\frac{m_p}{m} = \exp\left(\left(0.0015V - 0.2\right) v_{esc} + 0.0125V - 0.25\right), \tag{4.5}$$

where all velocities are in units of km/s and $v_{esc} = 4.25$ km/s is Mercury's escape velocity. In the velocity range between 15 and 30 km/s, we use a linear interpolation between Equations 4.4 and 4.5. Figures 4.6, 4.7 and 4.8 illustrate the retained mass fraction, $1 - \frac{m_p}{m}$, for each comet and asteroid that impacts Mercury in our simulations and for the total dust flux. For impact velocities up to 45 km/s, at least 20% of material is retained on the surface. For impact velocities beyond 60 km/s, all impactor material is lost to space.

Taking into account the retained fraction of each comet, we estimate the total water flux at Mercury to be 0.0105×10^6 kg/yr for the primary comet simulation and 0.0106×10^6 kg/yr for the crosscheck comet simulation.

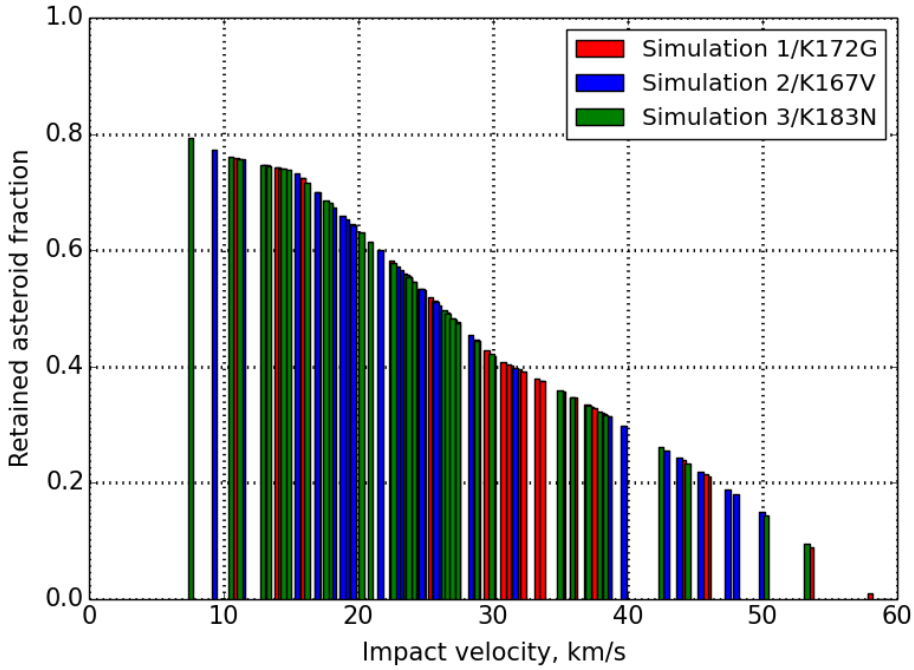

Figure 4.7: Retained mass fraction of each asteroid impacting Mercury in all three simulations. For impact velocities larger than 60 km/s, all impactor material (and hence all water) is lost to space.

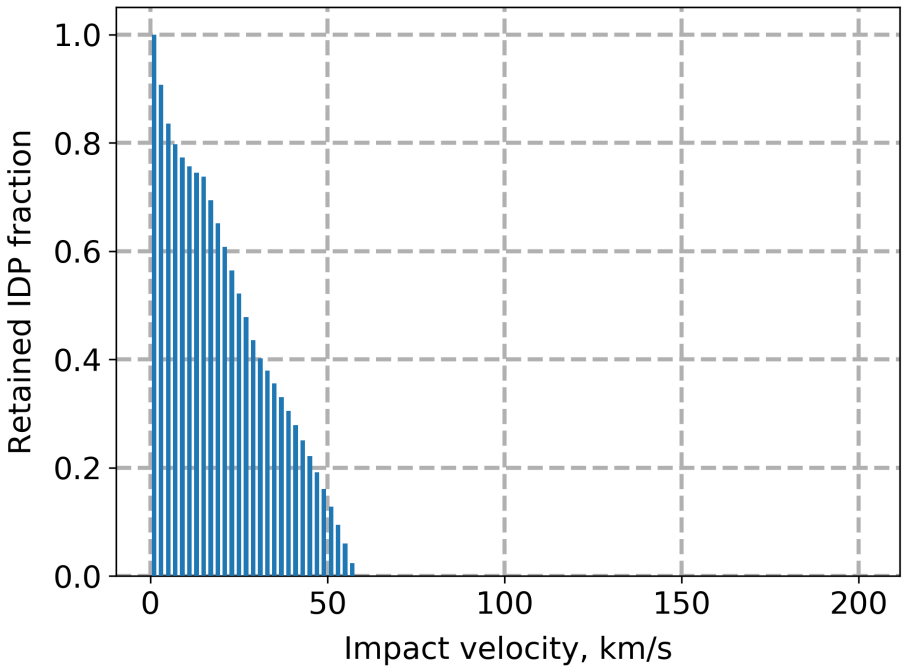

Figure 4.8: Retained mass fraction of interplanetary dust particles impacting Mercury. For impact velocities larger than 60 km/s, all impactor material (and hence all water) is lost to space.

Our final adopted cometary retained water flux is 0.0105×10^6 kg/yr. For the asteroids, we estimate the water flux at Mercury to be 0.008×10^6 kg/yr, 0.013×10^6 kg/yr and 0.074×10^6 kg/yr for the asteroid Simulation 1, Simulation 2, and Simulation 3 correspondingly as shown in Table 4.2. Our final adopted asteroid retained water flux is the harmonic mean of the range spanned by our results of 0.014×10^6 kg/yr within a factor of three. For the interplanetary dust particles, our estimated value of the retained water flux is 0.207×10^6 kg/yr.

4.5.2 Water loss during migration to cold traps

Impacts of asteroids, comets and IDPs are spread homogeneously over all latitudes of the planet.[1] Part of the water delivered by the impacts will reach the polar regions through migration processes. Butler et al. (1993); Butler (1997) have performed a Monte Carlo molecule migration simulation to study which fraction of volatiles will be captured in the cold traps of Mercury. Their simulations show that $\approx 5 - 15\%$ of the water molecules will survive to reach the cold polar regions before being dissociated by solar ultraviolet radiation. Combining the migration rates with our retained water fluxes it follows that 1×10^3 kg/yr of asteroid-borne water will be trapped in the permanently shadowed regions, analogously 1×10^3 kg/yr of comet-borne water and 16×10^3 kg/yr of IDP-borne water. Our final adopted values are the harmonic means of the ranges spanned by our results within a factor of several.

4.6 DISCUSSION

Asteroids, comets, and IDPs are possible exogenous sources of water on Mercury. In the previous sections, we find that asteroids, comets and IDPs deliver $\sim 1 \times 10^3$ kg/yr, $\sim 1 \times 10^3$ kg/yr and $\sim 16 \times 10^3$ kg/yr within a factor of several of water to Mercury's polar regions, respectively. IDPs are the dominant source of water, asteroids deliver an order of magnitude less, and comets deliver the least.

IDP fluxes on Mercury have also been calculated by Moses et al. (1999), Borin et al. (2017) and Pokorný et al. (2018). Our estimate for the total IDP influx on Mercury, 6×10^6 kg/yr, is a factor of 2 lower than the value

[1] Based on MESSENGER observations, Fassett et al. (2012) demonstrated that impact craters on Mercury show a non-uniform distribution in longitude. While we do not attempt to explain that finding, it does not influence our analysis in this section. A hypothetical inhomogeneity in latitude, which is not found, would.

	Incoming flux	Retained flux	Post-migration flux
Simulation 1	$0.021 \pm 0.009 \times 10^6$	0.008×10^6	$(0.4 - 1.2) \times 10^3$
Simulation 2	$0.023 \pm 0.009 \times 10^6$	0.013×10^6	$(0.7 - 2.0) \times 10^3$
Simulation 3	$0.430 \pm 0.190 \times 10^6$	0.074×10^6	$(3.7 - 11.1) \times 10^3$
Final value	0.032×10^6	0.014×10^6	1.05×10^3

Table 4.2: For each of our three asteroid simulations, we list the corresponding water fluxes before impact (column 1), after post-impact ejection (column 2), and the water flux that successfully migrates to the polar cold traps (column 3). All values are in units of kg/yr. In the last row, we provide our final adopted values of each column, where we adopt the harmonic mean of the ranges spanned by our results; uncertainties are a factor of $4 - 5$ in column 1, a factor of ~ 3 in column 2, and a factor of ~ 5 in column 3.

of Moses et al. (1999) of 10^7 kg/yr, a factor of 40 lower than the value of Borin et al. (2017) of 2×10^8 kg/yr and in good agreement with the estimate of 4.4×10^6 kg/yr by Pokorný et al. (2018). The difference relative to Moses et al. (1999) can easily be explained by the different adopted values for the measured IDP rate on Earth, reconciling our results. The origin of the difference relative to Borin et al. (2017) is not clear to us. We do wish to point out, though, that our result for Mercury is lower than that for Earth, while it is the other way around for Borin et al.. The gravitational cross-section of the Earth is $\simeq$7 times larger than that of Mercury, making our result more plausible.

Our delivery rates due to asteroid and comet impacts can be compared to results by Moses et al. (1999). They found that asteroids would deliver $(0.4 - 20) \times 10^{13}$ kg of ice in 3.5 Gyr, consistent with our estimate of $\sim 0.4 \times 10^{13}$ kg. Our results should be more accurate than those of Moses et al. (1999), chiefly because they are based on the known distribution of asteroid orbits as of 2018 rather than an extrapolation of the 1994 dataset. Furthermore, our probabilistic approach to define water-rich asteroids is more advanced than the flat 5% water content assumed by Moses et al. (1999).

For comets, Moses et al. (1999) treat Jupiter-family comets and Halley-type comets separately. For the former, they estimate a delivery rate of $(0.1 - 200) \times 10^{13}$ kg in 3.5 Gyr, and $(0.2 - 20) \times 10^{13}$ kg in 3.5 Gyr for the latter. Our estimate for water delivered by the entire comet population is $\sim 0.4 \times 10^{13}$ kg in 3.5 Gyr. While these results do agree at the lower range of the quoted uncertainty intervals, much larger delivery rates are allowed by Moses et al. (1999) than by our results. We attribute this chiefly to their large model-dependent correction factors accounting for the observational incompleteness of comets. Compared to them, we benefit of 20 years of systematic sky surveys looking for asteroids (and occasionally discovering comets as bycatch). This should largely eliminate observational incompleteness for large Jupiter-Family Comets with their orbital periods of 20 years or less; correspondingly, we should estimate the delivery rate due to Jupiter-Family Comets rather accurately (note that delivery is dominated by the largest impactors). Delivery due to longer-period comets would be underestimated in our model, on the other hand. However, long-period comets impact at large relative velocities, causing most water to be lost to space.

Based on the radar observations the total mass of water ice on Mercury's poles was calculated to be $4 \times 10^{13} - 8 \times 10^{14}$ kg (Moses et al., 1999). Using the MESSENGER observations it has been shown that the total mass of water on Mercury's poles is 2.1×10^{13} to 1.4×10^{15} kg (Lawrence et al.,

2013), consistent with the radar result. MESSENGER found the surface area of the permanently shadowed regions around the north pole to be $(1.25 - 1.46) \times 10^{10}$ m^2 and $(4.3 \pm 1.4) \times 10^{10}$ m^2 around the south pole. Combining the neutron and radar data from the MESSENGER spacecraft, the water ice origin of the radar-reflective deposits was confirmed for the North polar region (NS was not sensitive to the South due to the spacecraft's eccentric orbit). The total amount of water in the deposits is calculated based on the assumption that the South pole deposits have the same composition (Lawrence et al., 2013). Additionally, estimates of the deposit mass, based on MESSENGER observations, assume that the deposits are between 0.5 m and 20 m deep. That layer depth follows from models of surface modification processes (Crider & Killen, 2005) and from models of the radar scattering (Butler et al., 1993), not from MESSENGER data directly.

We find that impacts of IDPs, asteroids, and comets deliver $\sim 18 \times 10^3$ kg/yr of water to Mercury's poles. This is easily enough to explain the observational lower limit on the ice-layer thickness of 2.1×10^{13} kg; delivery would take ~ 1 Gyr. While our analysis does not rule out any other sources of water ice on Mercury, we do show that none are needed to explain the (lower limits on the) data available today. Over 3.5 Gyr impacts of dust, asteroids and comets would deliver up to 6×10^{13} kg. More is allowed but not required by the data. Should evidence for more water ice than 6×10^{13} kg be found in the future, this would necessitate additional water sources beyond impacts.

IDPs, comets, and C-type asteroids are not only rich in water but also in organic molecules. While an endogenous contribution to Mercury's water cannot be ruled out, there is no plausible endogenous formation mechanism for organics; therefore any positive detection of organics would prove the exogenous origin of the bright and dark deposits (Zhang & Paige, 2009).

For a better understanding of the nature and the origin of the dark and bright deposits in the polar regions of Mercury, more observational data are needed. For example, investigating various isotopic ratios, like D/H and ^{14}N/^{15}N for the Earth, may be a way to constrain the origins of Mercury's water. The joint ESA-JAXA mission BepiColombo, launched in 2018 and scheduled to arrive at Mercury in 2025, will guide further exploration. BepiColombo's polar orbit will be much less eccentric than that of MESSENGER. This will allow to perform elemental measurements of the southern hemisphere that were made with poor spatial resolution or even not possible before. Importantly for our purposes, BepiColombo carries the Mercury Gamma-Ray and Neutron Spectrometer (MGNS), similar to

MESSSENGER's NS but at higher resolution. MGNS will map water across the entire surface of Mercury, including the Southern polar regions, down to a depth of 1–2 m (Mitrofanov et al., 2010) and will clarify if the Southern polar region is indeed as water-rich as its Northern counterpart.

4.7 CONCLUSIONS

IDPs, asteroids and comets play an important role in the formation process of the dark and bright deposits in the polar regions of Mercury that have been associated with water ice. While other sources are not ruled out by our analysis, we show that impacts can deliver a sufficient amount of water to Mercury's polar regions to explain the available observational data; delivery would take ~ 1 Gyr. IDPs deliver more water than asteroids and comets combined.

ACKNOWLEDGEMENTS

We are thankful to *Petr Pokorny* for providing us impact velocity distribution of IDPs and useful discussions, *David E. Kaufmann* for valuable help with RMVS/Swifter, *Cecile Engrand* and *Mikhail Zelensky* for input on the water fraction of IDPs.

This research has made use of data and/or services provided by the International Astronomical Union's Minor Planet Center.

We would like to thank the Center for Information Technology of the University of Groningen for their support and for providing access to the Peregrine high performance computing cluster.

The authors thank the two anonymous reviewers for their thoughtful comments, which significantly improved the manuscript.